

Article

Nanogap Plasmon Resonator: An Analytical Model

Andrey K. Sarychev ¹, Grégory Barbillon ^{2,*} and Andrey Ivanov ^{1,*}

¹ Institute for Theoretical and Applied Electrodynamics, Russian Academy of Sciences, 125412 Moscow, Russia; sarychev_andrey@yahoo.com

² EPF-Engineering School, 55 Avenue du Président Wilson, 94230 Cachan, France

* Correspondence: gregory.barbillon@epf.fr (G.B.); av.ivanov@physics.msu.ru (A.I.)

Abstract: Generic, analytical equations are suggested for the localized plasmon excited in a narrow gap formed between a metal/dielectric cylinder and a metal surface. The local distribution of the electric field was found by employing the quasi-static approximation. A strong electric field can be achieved in the nanogap in the optical and infrared frequency regimes. The maximum electric field was reached when the incident light was in resonance with the mode of the plasmon gap and can be expressed in terms of the incident field E_0 as $|E_{max}/E_0| \propto |\epsilon_m| \delta^{-2}$ with $\delta = \Im \epsilon_m / \Re \epsilon_m$. This aspect of the maximum field achievable in the nanogap can be enhanced by many orders of magnitude. The results of the analytical model were in relatively good agreement with a known theoretical model and the experimental results of surface-enhanced Raman scattering (SERS). The narrow gap resonator seems to be a powerful and flexible tool for different spectroscopies such as SERS and infrared absorption.

Keywords: plasmon nanogap resonator; plasmonic devices; plasmonic sensing; electric field enhancement



Citation: Sarychev, A.K.; Barbillon, G.; Ivanov, A. Nanogap Plasmon Resonator: An Analytical Model. *Appl. Sci.* **2023**, *13*, 12882. <https://doi.org/10.3390/app132312882>

Academic Editor: Michael (Misha) Sumetsky

Received: 25 October 2023

Revised: 22 November 2023

Accepted: 27 November 2023

Published: 30 November 2023



Copyright: © 2023 by the authors. Licensee MDPI, Basel, Switzerland. This article is an open access article distributed under the terms and conditions of the Creative Commons Attribution (CC BY) license (<https://creativecommons.org/licenses/by/4.0/>).

1. Introduction

The calculation of the electric field in the gap between two metallic cylinders is a classical problem in electrodynamics. However, the metal permittivity is typically negative in the optical spectral range, and plasmons are excited between the cylinders, which provide a great enhancement of the local electric field in the gap [1]. Later, it was shown that the large optical field fluctuations in random semicontinuous metallic films were due to the local field concentration in between large metallic clusters [2]. The two metallic nanostructures supporting localized plasmons behave as an open resonator when they are separated by a spatial gap. Exact spectral control is achieved by changing the nanogap's width [3,4].

Echtermeyer et al. reported the use of plasmon nanogaps in order to increase the sensitivity of photodetectors [5]. Halas' group showed that the frequency transformation due to the non-linearity was determined by the value of the local electric field and its spatial localization within the gap [6]. The physical processes that are crucially important for sensing can be observed in quantum plasmonics for gaps having a subnanometric size between the metallic particles [7]. Baumberg's group reported the use of graphene to tune the subnanometric size of the gaps within metallic dimers [8]. Metallic nanoparticle arrays with a 1–5 nm range of the gap size were prepared by using the atomic layer deposition of aluminum oxide, allowing the control of this gap size [9]. Several groups have demonstrated the achievement of strong electric fields thanks to plasmonic nanoparticles/nanostructures deposited on a metallic film serving as a mirror [10–16]. Furthermore, a great number of research groups have studied the coupling of plasmonic nanoparticles with nanogaps or subnanogaps [9,17–34]. These various groups have theoretically and experimentally investigated great enhancements of the electromagnetic field concerning the coupling of these plasmonic nanoparticles with nanogaps (or subnanogaps) [35–44]. Xomalis et al.

reported the generation of high-order modes of plasmons obtained with gold nanoparticles deposited on a gold disk of a micrometric size with a gap between them, which can be adjusted by the dimensions of the molecule serving as a spacer [30]. Ding et al. presented studies based on the metasurfaces of a gap plasmon composed of nanostructure arrays and a thick film of metal spaced apart by a thin film of dielectric, thus permitting the parameter adjustment of the reflected light (i.e., polarization, amplitude, and phase) [45]. Furthermore, the principle of the gap plasmon can be applied to several domains, such as strong coupling between the plasmon and exciton [46,47], the spectroscopy of infrared absorption enhanced by the surface [48], the improvement of electroluminescence [49] and fluorescence [50], non-local effects [51], hyperspectral imaging [52], and the detection of hot electrons [53]. A strong motivation for the investigation of gap plasmons is the effect of surface-enhanced Raman scattering (SERS), which relies on plasmonic enhancement to enable the identification of trace molecules captured within gaps [54]. SERS is extremely important for medical diagnostics, for instance for cancer detection, imaging, and therapy, drug delivery, and the quantitative control of biomarkers, including glycosylated proteins and cardiovascular biomarkers, and viruses [34,55–59]. For instance, Sarychev et al. demonstrated a sensitive detection of less than 1 pg of a biological molecule (the spike glycoprotein of SARS-CoV-2) by employing a nanometric cavity formed by an Ag film and a layer of a receptor-binding domain of this glycoprotein [34]. Li et al. reported a significant improvement of the SERS effect by employing a nanocavity of a size comparable to the wavelength of excitation and composed of a gold film and a silver nanostructure (nanoframe) separated by the layer of molecules to be detected [31]. In the majority of the studies described previously, the theoretical aspects have generally been addressed by using numerical simulations.

In this work, we propose an analytical model of plasmons excited in an ultra-narrow gap formed by a metallic cylinder on a metallic surface for different metals. We found the resonance conditions in which it is possible to achieve the limit of the electromagnetic field both inside and in the vicinity of the gap. This will increase the sensitivity of SERS probing, as well as that of other existing surface-enhanced spectroscopies. In Section 2, we describe the analytical model. Then, in Section 3, we compare our analytical model to another theoretical model developed by Pendry's group to the experimental results obtained by Zayats' group, as well as to the simulation results obtained by the group of Bozhevolnyi and by Li et al.

2. Analytical Model

We considered two parallel metallic cylinders whose respective radii were a and $a_1 > a$, which were separated by a distance $d + d_1$, so that the spacing between the cylinder axes was $a + d + a_1 + d_1$. The x -axis connects the cylinders' centers, which have the coordinates $\{x, y\} = \{a + d, 0\}$ and $\{-a_1 - d_1, 0\}$, as displayed in Figure 1. In order to assess the electric field located in the nanogap lit with an incident light (see Figure 1d), alternative coordinates (u and v) were employed, facilitating the introduction of the complex variables z and w associated with the following equation:

$$z = L \tanh \frac{w}{2} \quad (1)$$

with z corresponding to $x + iy$, w corresponding to $u + iv$, and L equal to:

$$L = \sqrt{d(2a + d)} \quad (2)$$

where d is the length between the cylinder surface (named a) and the origin of the coordinate system. Note that a , a_1 , and L fully define the system geometry, if we define $d_1 = \sqrt{a_1^2 + L^2} - a_1 < d$. The electrodynamics of two parallel cylinders is defined by their radii a , $a_1 > a$ and the distance between the cylinders, which equals $d + d_1 = \sqrt{a^2 + L^2} - a + \sqrt{a_1^2 + L^2} - a_1 \approx L^2(a + a_1)/(2aa_1)$. A particular value of d or d_1 simply defines the position of the origin of the coordinates as soon as the values a ,

a_1 , and L are given. The length L corresponds to the characteristic length of the electric field variation in the gap, as shown below. In the transition from z to w , the whole plane $\{x, y\}$ transforms to the strip $-\infty < u < \infty, -\pi < v < \pi$. The surfaces of the cylinders “ a ” and “ a_1 ” are transformed to the vertical lines $u_d = \ln[(a + d)/(a - d)] > 0$ and $u_{d_1} = -\ln[(a_1 + d_1)/(a_1 - d_1)] < 0$ (Figure 1).

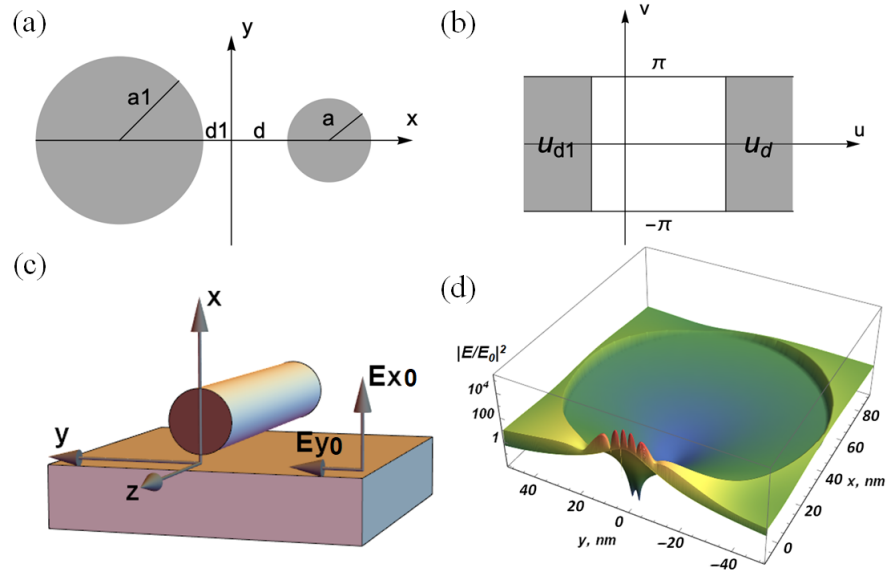


Figure 1. The design of cylindrical nanoparticle-on-mirror cavity. (a,b) Conformal map of two cylinders into the $u - v$ strip; (c) metallic cylinder above the metal plate; the electromagnetic wave is incident from the top; (d) electric field between Ag plate and cylinder with a radius of $a = 50$ nm and the gap $d = 0.5$ nm calculated at the excitation wavelength of $\lambda = 405$ nm.

The entire outer space of the cylinders shrunk into the rectangular $[u_{d_1} < u < u_d, -\pi < v < \pi]$. The approach was similar to the map used in [35,60]. The solution of the Laplace equation in the rectangle can be presented as a sum of functions $f_{Rc}^{(q)} = e^{-qu} \cos qv, f_{Rs}^{(q)} = e^{-qu} \sin qv, f_{Lc}^{(q)} = e^{qu} \cos qv, f_{Ls}^{(q)} = e^{qu} \sin qv, q = 1, 2, \dots$

$$\varphi^G(u, v) = \varphi_0 + \sum_{q=1}^{\infty} [A_1^{(q)} f_{Rc}^{(q)} + A_2^{(q)} f_{Rs}^{(q)} + A_3^{(q)} f_{Lc}^{(q)} + A_4^{(q)} f_{Ls}^{(q)}] \tag{3}$$

where φ_0 is the potential of the external electric field. We assumed that the electric field concentrates in the nanogap whose size is much smaller than the wavelength of the incident light $d + d_1 \ll \lambda$. The electric potentials in the “ a ” and “ a_1 ” cylinders are given by the following expressions, respectively:

$$\varphi^R(u, v) = \varphi_0 + \sum_{q=1}^{\infty} [B_1^{(q)} f_{Rc}^{(q)} + B_2^{(q)} f_{Rs}^{(q)}], \quad u > u_d \tag{4}$$

$$\varphi^L(u, v) = \varphi_0 + \sum_{q=1}^{\infty} [B_3^{(q)} f_{Lc}^{(q)} + B_4^{(q)} f_{Ls}^{(q)}], \quad u < u_{d_1} \tag{5}$$

The components of the electric field in $\{u, v\}$ space $\{E_u, E_v\} = -\nabla_w \varphi = -\{\partial\varphi/\partial u, \partial\varphi/\partial v\}$ are complex since the metal permittivity is complex. The electric field in $\{x, y\}$ space is equal to $\{E_x, E_y\} = \hat{J}\{E_u, E_v\}$, where the Jacobian \hat{J} was obtained from the derivative $w_z = dw/dz$, namely $J_{11} = J_{22} = \Re w_z, J_{21} = -J_{12} = \Im w_z$. The coefficients $A^{(q)}$ and $B^{(q)}$ in the Equations (3)–(5) were found from the boundary conditions for the electric

fields $E^R = -\nabla_w \varphi^R$, $E^G = -\nabla_w \varphi^G$, and $E^L = -\nabla_w \varphi^L$ at the surface of the “ a ” and “ a_1 ” cylinders:

$$E_v^R = E_v^G, \varepsilon_m E_u^R = \varepsilon_d E_u^G, u = u_d \tag{6}$$

$$E_v^L = E_v^G, \varepsilon_{m_1} E_u^L = \varepsilon_d E_u^G, u = u_{d_1} \tag{7}$$

where ε_m , ε_d , and ε_{m_1} are the permittivities of the “ a ” cylinder, the outer space, and the “ a_1 ” cylinder, respectively. We expanded the external field $E_0 = -\nabla \varphi_0 = \{E_{0x}, E_{0y}\}$ in a series of functions $f_{Rc}^{(q)}, f_{Rs}^{(q)}, f_{Lc}^{(q)}, f_{Ls}^{(q)}$. For the simplest case of the constant external field, the expansion:

$$\{E_{0u}, E_{0v}\} = \sum_q \{E_{0u}^{(q)}, E_{0v}^{(q)}\} \tag{8}$$

has the following form:

$$\{E_{0u}^{(q)}, E_{0v}^{(q)}\} = -2L(-1)^q q \times \begin{cases} E_{0x} f_{Rc}^{(q)} - E_{0y} f_{Rs}^{(q)}, E_{0x} f_{Rs}^{(q)} + E_{0y} f_{Rc}^{(q)}, u > 0 \\ E_{0x} f_{Lc}^{(q)} + E_{0y} f_{Ls}^{(q)}, E_{0y} f_{Lc}^{(q)} - E_{0x} f_{Ls}^{(q)}, u < 0 \end{cases} \tag{9}$$

where $q = 1, 2, \dots$. We substituted the above equation into the boundary Equation (6) for the surface of the “ a ” cylinder and assimilated the coefficients to the same $f^{(q)}$ functions by obtaining the following equations for the coefficients $\{A^{(q)}, B^{(q)}\}$ in the Equations (3)–(5):

$$\varepsilon_d (A_3^{(q)} + A_1^{(q)} g^{2q}) - \varepsilon_m B_1^{(q)} = E_{0x} (\varepsilon_m - \varepsilon_d), \tag{10}$$

$$\varepsilon_d (A_4^{(q)} - A_2^{(q)} g^{2q}) - \varepsilon_m B_2^{(q)} = E_{0y} (\varepsilon_m - \varepsilon_d), \tag{11}$$

$$A_2^{(q)} g^{2q} + A_4^{(q)} - B_2^{(q)} = A_1^{(q)} g^{2q} - A_3^{(q)} + B_1^{(q)} = 0 \tag{12}$$

where $g = (L + d)/(L - d)$. By matching the electric field and the displacement on the surface of the “ a_1 ” cylinder, we obtain from the Equation (7):

$$\varepsilon_d (A_1^{(q)} + A_3^{(q)} g_1^{2q}) - \varepsilon_{m_1} B_3^{(q)} = E_{0x} (\varepsilon_{m_1} - \varepsilon_d), \tag{13}$$

$$\varepsilon_d (A_2^{(q)} - A_4^{(q)} g_1^{2q}) - \varepsilon_{m_1} B_4^{(q)} = E_{0y} (\varepsilon_{m_1} - \varepsilon_d), \tag{14}$$

$$A_4^{(q)} g_1^{2q} + A_2^{(q)} - B_4^{(q)} = A_3^{(q)} g_1^{2q} - A_1^{(q)} + B_3^{(q)} = 0 \tag{15}$$

where $g_1 = (L + d_1)/(L - d_1)$. Setting the determinant of Equations (10)–(12) and (13)–(15) to zero gives the “ q ” resonance condition. The cylinders with the same permittivity $\varepsilon_{m_1} = \varepsilon_m$ resonate when $(gg_1)^{2q} (\varepsilon_d + \varepsilon_m)^2 - (\varepsilon_m - \varepsilon_d)^2 = 0$. The first term dominates when the distance $d + d_1$ between the cylinders increases and $gg_1 \rightarrow \infty$. Then, all resonant frequencies $\omega_r^{(q)}$ collapse into a single value $\omega_r^{(1)}$ given by the well-known equation $\Re[\varepsilon_d(\omega_r^{(1)}) + \varepsilon_m(\omega_r^{(1)})] = 0$ for the plasmon resonance in a metallic cylinder. On the other hand, when the gap size vanishes $d + d_1 \rightarrow 0$, the factor $gg_1 \rightarrow 1$ from above and the resonance frequencies $\omega_r^{(q)}$ spread out from $\omega_r^{(1)}$ to the minimum resonance frequency estimated from the equation $\varepsilon_m(\omega_r^{(m)}) \simeq -\frac{2\varepsilon_d a a_1}{L(a+a_1)} \rightarrow -\infty$. The real part of the permittivity of silver, gold, and many other metals is well described by the Drude formula in the red and infrared spectral range $\Re \varepsilon_m(\omega) \propto -(\omega_p/\omega)^2$ [61] and the minimal resonant frequency $\omega_r^{(m)} \propto \omega_p(d/a)^{1/4} \ll \omega_p$.

Observing plasmon resonance between the metal cylinders is a challenging experimental problem involving positioning two nanocylinders parallel to each other at a nanometric distance. Yet, the investigation of the plasmon resonance in the metallic nanocylinder placed at a nanodistance above a flat metallic surface (i.e., $a_1 = \infty$) is the focus of current experimental studies. In order to evaluate the electric field located within this nanogap, the limit case was employed (i.e., $a_1 \rightarrow \infty$ and $d_1 \rightarrow 0$). The electric field (named E_0) had a fixed

value at the level of the cylinder surface a_1 (far from the cylinder a). Thus, all expressions of the electric field are expressed in terms of E_0 . For the limit case ($a_1 \rightarrow \infty$), E_0 corresponds to that attached to the surface of the metal plate (i.e., at $x = 0$, $a \ll |y|$; see Figure 1c). From there, the electric field $E(x, y)$ was assessed at the central coordinates (i.e., $(x, y) = (0, 0)$ and $(u, v) = (0, 0)$), and its value was maximal, as depicted in Figure 1c,d. Thus, the Jacobian \hat{J} simplifies to the scalar quantity L , and the expression of $E_{x,y}$ was determined by solving the Equations (10)–(12) and (13)–(14). The field equation is simplified in the center of coordinates, namely

$$E(x = 0, y = 0) = \left\{ E_{x0} \left[1 + \frac{8\varepsilon_{m1}\Sigma}{\varepsilon_d - \varepsilon_m} \right], E_{y0} \left[1 - \frac{8\varepsilon_d\Sigma}{\varepsilon_d - \varepsilon_m} \right] \right\}, \tag{16}$$

$$\Sigma = \sum_{q=1}^{\infty} \frac{(-1)^q q h}{(b + 1)^q - h}, \quad h = \frac{(\varepsilon_d - \varepsilon_m)(\varepsilon_d - \varepsilon_{m1})}{(\varepsilon_d + \varepsilon_m)(\varepsilon_d + \varepsilon_{m1})}, \tag{17}$$

$$b = (d + L)(2a + d + L)/a^2 \simeq \sqrt{8d/a} \tag{18}$$

where ε_m , ε_{m1} , and ε_d are the permittivities of the cylinder, metal plate, and outer space, respectively. a and d are the cylinder radius and the gap size, respectively. The last approximation in the Equation (18) holds for $d \ll a$. The system resonates if a denominator in the first equation in (17) almost vanishes, i.e., the dimensionless parameter $\Re h > 1$ and the loss factor $\kappa = \Im h/|h| \simeq 2\varepsilon_d \left(\Im \varepsilon_m |\varepsilon_m|^{-2} + \Im \varepsilon_{m1} |\varepsilon_{m1}|^{-2} \right) \ll 1$ for $|\varepsilon_m|, |\varepsilon_{m1}| \gg \varepsilon_d$.

Despite the simplicity of the Equations (16) and (17), the gap field has a rather rich behavior when the gap vanishes, i.e., $b \rightarrow 0$. Suppose that the parameter $\Re h < 1$, then the denominator $n^{(q)} = (b + 1)^q - h$ in the sum Σ in the Equation (17) is not close to zero for all the values of q , and hence, it can be linearized as $n^{(q)} \simeq b_1 q - h_1$, where $h_1 = h - 1$, $\Re h_1 < 0$, $b_1 = \log(1 + b) \simeq b$. Then, the sum Σ in the Equation (17) is approximated as

$$\Sigma \simeq S(h_1, b_1) = \sum_q^{\infty} (-1)^q q / (b_1 q - h_1) \tag{19}$$

which can be solved by the Laplace transformation and Abel regularization. The function S has a simple integral presentation:

$$\Sigma \simeq S = \frac{h_1(\psi_1 - \psi_2) + b_1}{2b_1^2} = - \int_0^1 \frac{x^{-\frac{h_1}{b_1}} dx}{(x + 1)^2 b_1} \tag{20}$$

where $\psi_1 = \psi\left(\frac{b_1 - h_1}{2b_1}\right)$, $\psi_2 = \psi\left(-\frac{h_1}{2b_1}\right)$ and $\psi = \Gamma'/\Gamma$ is the polygamma function. The sum is approximated as $\Sigma \simeq -\frac{1}{4(b_1 - h_1)} \left(\frac{b_1}{2b_1 - h_1} + 1 \right) \rightarrow \frac{1}{4h_1}$ for the fixed h_1 and $|b_1/h_1| \rightarrow 0$. In other words, the electric field tends towards a finite value when the gap between the cylinder and the plate vanishes. The integral (20) converges for $\Re h_1/b_1 < 1$. In the opposite case, one of the denominators $n^{(q)}$ in the sum Σ of the Equation (17) vanishes for $q = q_c = \log h / \log(1 + b)$. We linearized the denominator at this point, obtaining $n^{(q)} \simeq [dn^{(q)}/dq](q - q_c) = qb_2 - h_2$, where $b_2 = h \log(1 + b)$ and $h_2 = h \log h$. Therefore, the sum S in the Equation (17) is still given by the Equation (19), where the parameters b_1 and h_1 are replaced by b_2 and h_2 . The terms in Σ with numbers close to $q_1 = \Re q_c$ have the maximum impact on the sum Σ . The analytical continuation of the function $S(b_2, h_2)$ to the domain $\Re[h_2/b_2] < 0$ gives:

$$\Sigma \simeq -\frac{x^2}{b_2 \sin(x)} - S(-h_2, b_2) \tag{21}$$

where $x = \pi h_2/b_2 = \frac{\pi \log h}{\log(1+b)} \simeq \frac{\pi \log |h|}{\log(1+b)} + i \frac{\pi \kappa}{\log(1+b)}$, $S(-h_2, b_2)$ is still given by the integral in the Equation (20). The first resonance term of the Equation (21) determines the singular

behavior of the field when the loss factor $\kappa \ll 1$. Suppose that the frequency is fixed, then the sum $|\Sigma|$ oscillates as a function of $b \ll \log|h|$ (see Figure 2).

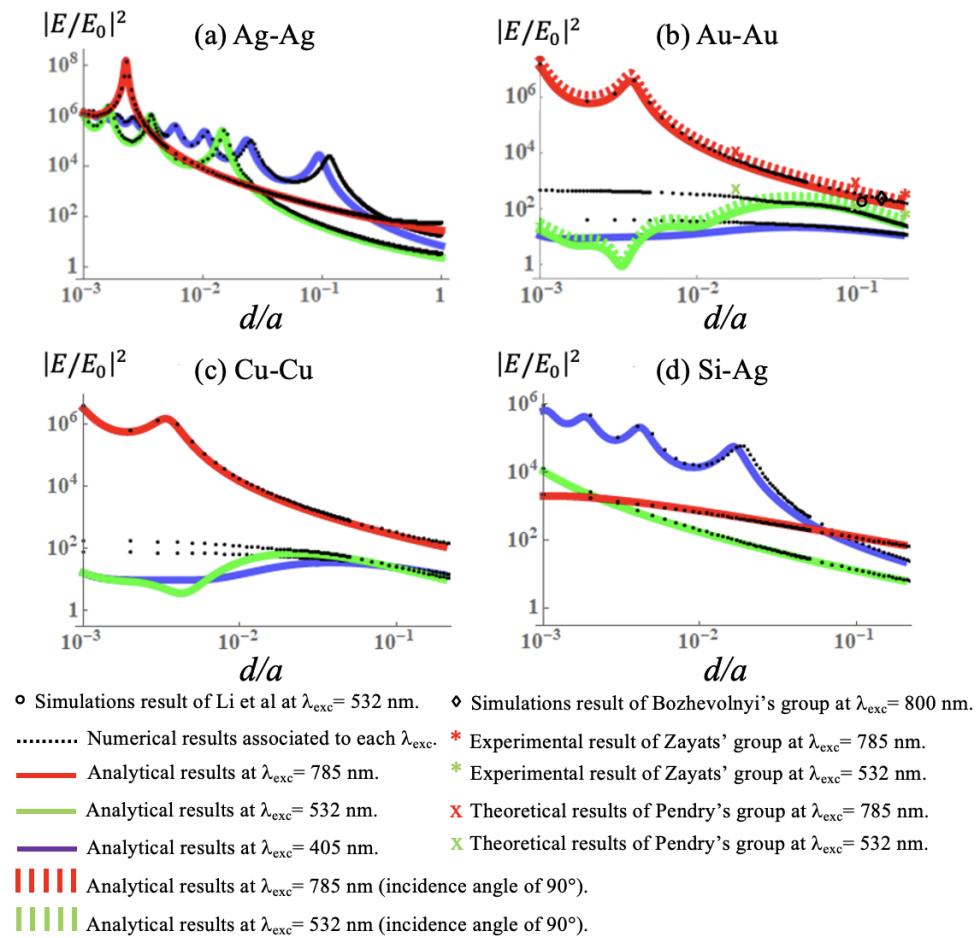


Figure 2. Comparison of analytical (lines) and numerical (dots) maximum electric field intensities $|E/E_0|^2$ in the gap (see Figure 1) between (a) the Ag cylinder and the Ag surface, (b) the Au cylinder and the Au surface, (c) the Cu cylinder and the Cu surface, and (d) the Si cylinder and the Ag surface. Red, green, and blue colors correspond to the excitation wavelengths (λ_{exc}) of 785 nm, 532 nm, and 405 nm, respectively. The excitation beam has an incidence angle of 45° and a p -polarization. In (b), the stars and crosses represent, respectively, the experimental results obtained by Zayats' group and the theoretical results obtained by Pendry's group, for the excitation wavelengths of 785 nm (red) and 532 nm (green). The dashed lines correspond to the analytical results obtained with an incidence angle of 90° for the excitation beam. The black diamond and the black ring correspond to the simulation results obtained by Bozhevolnyi's group and by Li et al., respectively. The results are shown in logarithmic scale. The value of the field $|E/E_0|^2$ only depends on the ratio d/a in the quasi-static approach used in our analytical theory. For the computer simulations, the diameter of the cylinder is $2a = 20$ nm.

The oscillation period decreases with the decrease of the gap size. The local maxima $|\Sigma|_m$ are achieved when $\Re x = m\pi$. The value of these maxima is given by the following expression:

$$|\Sigma|_m \simeq \frac{\pi m^2}{|h_2|} \sinh\left(\frac{\pi m \kappa}{\log|h|}\right)^{-1} \quad (22)$$

This value increases linearly with the number m : $|\Sigma|_m \propto m/\kappa$ achieving the absolute maximum for $m = m_{mx} \simeq \log|h|/\pi\kappa$, namely $|\Sigma|_{mx} \simeq \log|h|/(\pi\kappa^2|h|)$. The oscillations collapse with a further decrease of the gap due to the losses in the system, and $|\Sigma|$ drops

down exponentially as a function of b . By substituting $|\Sigma|_{mx}$ into the Equation (16), we obtain the estimate of the limit of the electric field:

$$|E_{mx}|^2 \simeq \frac{64|h|^4 \log^2 |h|}{\pi^2(\Im h)^4} |E_{00}|^2 \tag{23}$$

where the parameter h is given by Equation (17), $|E_{00}|^2 = |E_{0x}\epsilon_{m1}|^2 + |E_{0y}\epsilon_d|^2$, while ϵ_m , ϵ_{m1} , and ϵ_d are the permittivities of the metal cylinder, the metal plate, and the surrounding space, respectively. In the red and infrared spectral ranges, the permittivity of the metal is large in absolute value ($|\epsilon_m|, |\epsilon_{m1}| \gg \epsilon_d$, $\Im\epsilon_m/|\epsilon_m|, \Im\epsilon_{m1}/|\epsilon_{m1}| \ll 1$), and the Equation (23) is simplified:

$$|E_{mx}|^2 \propto \frac{|\epsilon_m^6| |\epsilon_{m1}^4| (|\epsilon_m| + |\epsilon_{m1}|)^2}{\epsilon_d^2 (|\epsilon_m^2| \Im\epsilon_{m1} + |\epsilon_{m1}^2| \Im\epsilon_m)^4} |E_{00}|^2 \tag{24}$$

The maximum enhancement of the field is estimated at $|E_{mx}| \propto |\epsilon_m|^3 \epsilon_d^{-1} (\Im\epsilon_m)^{-2} |E_0|$ in the gap between the cylinder and the plate made of the same metal. For instance, the field can be as large as $|E_{mx}| > 10^3 |E_0|$ in the gap between the silver plate and a silver cylinder for the green light $\lambda = 532$ nm (Figure 2a). This is an upper limit since the field can be restricted by the radiation loss and spatial dispersion of the electric charge in subnanometer gap [3].

3. Analytical Model vs. Simulations and Experiments

In any real SERS detection experiment, a layer of molecules to be investigated is placed in the gaps formed by metallic particles distributed on a metal mirror. In this work, numerical simulations (COMSOL) were employed to reproduce the periodic grating of the metallic nanocylinders, whose dimensions were, respectively, 10 nm and 50 nm for the radius a of the nanocylinder for each grating and 200 nm for the periodicity D for both gratings. The arrays of nanocylinders were deposited on a metallic surface, then illuminated by p -polarized light at a 45° angle of incidence comparable to the work of Moskovits' group [10]. To obtain the reflectance and electric field measurements, we employed periodic boundary conditions and periodic ports. The 2D model was set up for an unit cell of the grating, flanked by Floquet boundary conditions describing the periodicity. This means that the solution on one side of the unit is equal to the solution on the other side multiplied by a complex-valued phase factor. The phase shift between the boundaries was evaluated from the perpendicular component of the wave vector. Port conditions were used to specify the incident wave. The radius a of the nanocylinder was fixed, and the size of the nanogap d was a variable parameter. The electric field in the gap and the S-parameters were obtained by solving Maxwell's equations via the finite-element method. Comparing the results of these numerical simulations with the analytical model, a relatively good agreement was observed for the enhancement of the electric field within the nanogap (see Figure 2a–c). By considering a metal–semiconductor nanogap, significant values of the electric field within the latter can be achieved (see Figure 2d). The concentration of electromagnetic energy in the nanogaps can be noticed by a decrease in reflectance (see Figure 3b,d).

To compare our analytical model with the computer simulations described above, we set the electric field E_s at the point $x = d + 2a, y = 0$ on the surface of a cylinder and calculated the field $E(x, y)$ throughout space using our analytical theory. To simplify the consideration, the direct interaction between cylinders was neglected since the electric field was localized in the nanogaps of size $d \ll a$. Then, we averaged the field over the layer $0 < x < d + 2a$ and introduced the effective permittivities $\epsilon_{xx}^{(e)} = \langle \epsilon(x, y) E_x(x, y) \rangle / \langle E_x(x, y) \rangle$ and $\epsilon_{yy}^{(e)} = \langle \epsilon(x, y) E_y(x, y) \rangle / \langle E_y(x, y) \rangle$. An electromagnetic wave of amplitude E_{in} and the p -polarization arrives on the layer placed above the metal plate. Maxwell's equations were solved in terms of amplitude E_{in} in order to find an electromagnetic field in the

layer of thickness $d + 2a$ and permittivity $\hat{\epsilon}^{(e)}$. In particular, we found the electric field $E_0 = \{E_{x0}, E_{y0}\}$ at the interface between the layer and the metal plate (see Figure 1c). In the dilute case $a \ll D \ll \lambda$, the field E_0 was equal to the field that was on the metal surface without a cylinder, namely

$$E_0 = E_{in} \left\{ \frac{\epsilon_{m_1} \sin 2\theta}{\sqrt{\epsilon_d \epsilon_{m_1} - \epsilon_d^2 \sin^2 \theta} + \epsilon_{m_1} \cos \theta}, \frac{2 \cos \theta \sqrt{\epsilon_d \epsilon_{m_1} - \epsilon_d^2 \sin^2 \theta}}{\sqrt{\epsilon_d \epsilon_{m_1} - \epsilon_d^2 \sin^2 \theta} + \epsilon_{m_1} \cos \theta} \right\} \quad (25)$$

where θ is the angle of incidence. This field was introduced into Equation (16) in order to obtain the analytical estimate of the electric field in the nanogap. The theoretical results were consistent with full-scale computer simulations for small cylinders ($ka \ll 1$). The results of our quasi-static model extrapolated to $ka \sim 1$ were still in qualitative agreement with the computer simulations of “large” nanocylinders (see Figure 3). The agreement was better for a smaller gap size d and a higher plasmon resonance q . Indeed, our quasi-static theory worked better when the spatial scale of the electric field variance $L_q \sim L/q \sim \sqrt{ad}/q$ was much smaller than the wavelength λ . In this case, we believe that all other parts of the plasmonic system can be considered as an external environment by simply renormalizing the applied electric field. The model is valid when the plasmon size $L_q \sim \sqrt{ad}/q$ is less than the skin depth $L_q \ll \frac{1}{k\sqrt{|\epsilon_m|}}$. Figures 2 and 3 show that the largest field enhancement was obtained in the red and infrared spectral bands, where the optical loss in the metal was relatively low. On the other hand, the silver–silicon system resonated for $\lambda < 550$ nm when the parameter $\Re h$ in the Equation (17) became greater than one.

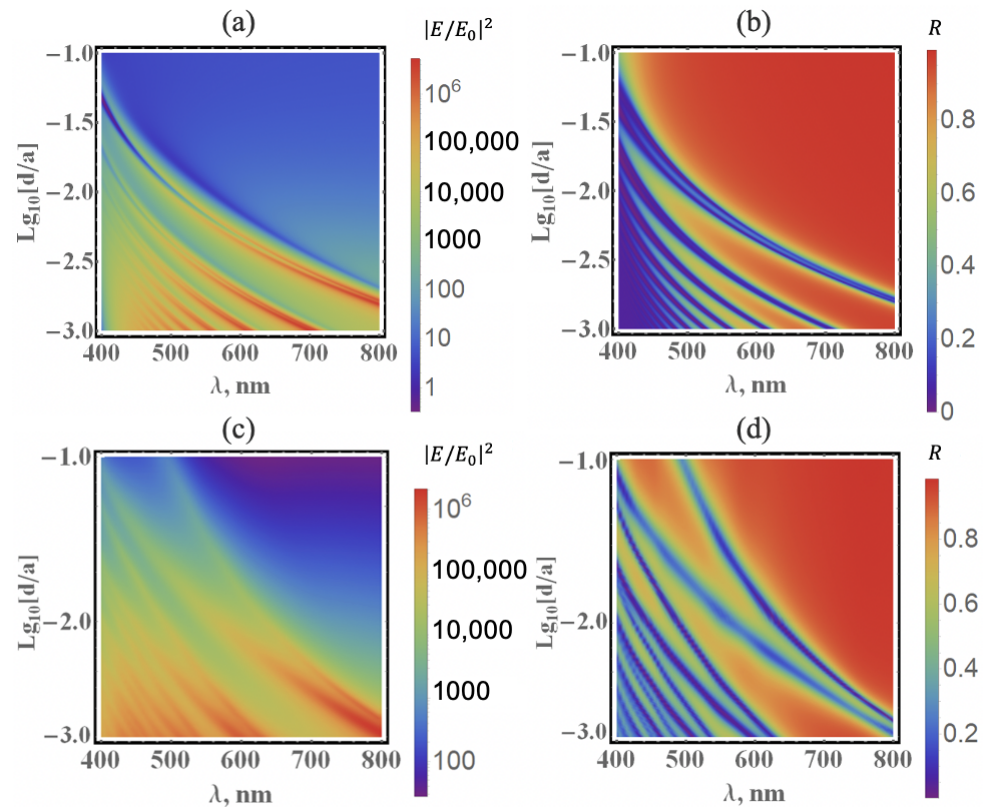


Figure 3. Analytical results in the gap between the Ag cylinder and the Ag surface as a function of wavelength and d/a ratio: (a) electric field intensity $|E/E_0|^2$ and (b) reflectance. Numerical results for the “large” silver cylinder with a radius of $a = 50$ nm and a period of $D = 200$ nm: (c) electric field intensity $|E/E_0|^2$ and (d) reflectance.

Moreover, we also compared our analytical model to other theoretical results obtained with a local analogue model (LAM) developed by Pendry's group [62]. A good agreement was obtained between our analytical model and the LAM of Pendry's group for the excitation wavelength of 785 nm (see the red line and red crosses in Figure 2b). For the excitation wavelength of 532 nm, our analytical model was still in relatively good agreement with the LAM (see the green line and green crosses in Figure 2b).

Furthermore, we compared our analytical model to the experimental results obtained on the enhancement factors of the SERS effect recorded by Zayats' group [63]. The nanostructures used for these experiments were arrays of gold dimers on a 50 nm-thick gold film, composed of two disks with a radius of 70 nm, height of 40 nm, and gap of 20 nm. They obtained $|E/E_0|^2$ ratios of 1.25×10^2 and 5.48×10^2 at the excitation wavelengths of 532 nm and 785 nm, respectively, for a corresponding d/a ratio of 0.29. We observed a good agreement between our analytical model and the experimental results recorded by Zayats' group (see the red/green lines and the red/green stars in Figure 2b). The small difference can be due to the difference in the incidence angle of the excitation beam between our analytical model (45° with respect to the surface normal) and the experimental results (normal incidence; the polarization of the excitation light was along the dimer direction). We analytically calculated the electric field intensity $|E/E_0|^2$ at the excitation wavelengths of 532 nm and 785 nm in the gap between the Au cylinder and the Au surface for the case considered by Zayats' group and Pendry's group, where the polarization of the excitation light was along the dimer direction. This configuration corresponded to ours at an incidence angle $\theta = 90^\circ$ with respect to the surface normal (see the red and green dashed lines in Figure 2b). In this case, $|E/E_0|^2$ was more enhanced and an even better agreement was reached with the above-mentioned results of Zayats and Pendry.

Besides, a comparison between our analytical model and the numerical simulations obtained by Bozhevolnyi's group was made [16]. The structure employed for these simulations was a disk on a 200 nm-thick gold film, the 40 nm gap between them of which was made by a layer of SiO_2 . The radius of the disk was 250 nm, and its height was 40 nm. They obtained an $|E/E_0|^2$ ratio of 2.25×10^2 at the excitation wavelength of 800 nm for a corresponding d/a ratio of 0.16. A good agreement was reached between our analytical model (at the excitation wavelength of 785 nm) and the simulation results obtained by Bozhevolnyi's group (see the black diamond in Figure 2b). Lastly, another comparison of our analytical model to the numerical simulations obtained by Li et al. was made [64]. The nanostructure employed for these simulations was a dimer composed of gold disks with a radius of 25 nm and a gap in between of 3 nm. They reached an $|E/E_0|^2$ ratio of 2×10^2 at the excitation wavelength of 532 nm for a corresponding d/a ratio of 0.12. A relatively good agreement between our analytical model and the simulations results obtained by Li et al. was achieved (see the black ring in Figure 2b).

The analytical model, as well as computer simulations predict a possible large enhancement in the local electric field between the dielectric cylinder and the metal mirror even in the absence of the plasmon resonance, as shown in Figure 2d for $\lambda = 532$ nm and 785 nm. We speculated that such enhancement of the non-resonant field was the result of the summation of many non-resonant gap modes. Non-resonant SERS was probably observed in recent experiments [34,59], where the Raman signal was detected from agglomerates of large protein molecules. The possibility of non-resonant SERS due to the formation of large molecular aggregates on the flat metal surface should be experimentally studied in more detail. Our model predicted a rather sophisticated behavior of the reflection from the metal nanocylinders distributed on the metal mirror, as shown in Figure 3b,d. By fitting the radii of the cylinders, the resonances can be tuned for particular frequencies. Then, the metal cylinder system can be used as a plasmonic paint of various colors. Indeed, various plasmon paints have attracted much attention in recent years (e.g., [65]).

4. Conclusions

In summary, we presented an analytical model of the plasmons excited in the gap between a metallic or dielectric nanocylinder and a metallic or dielectric plate. The resonance conditions for the gap plasmon were found as a function of the metal permittivity and the gap size. When the cylinder-on-mirror cavity was excited by the incident light, the electric field of the gap increased and oscillated with the decrease in the gap size to achieve its limit value. The excitation of gap plasmons led to dips in reflectance. The minimum “ q -th” of the reflectance corresponds to the excitation of the “ q -th”-order plasmon. Reflectance fluctuations have probably been observed, e.g., in experiments [3,66]. The quasi-static model qualitatively describes the field enhancement up to $ka \leq 1$, since the field is concentrated in the nanogap, whose size is much smaller than λ . Finally, we compared our analytical model with experimental results on the enhancement factors of the SERS effect, simulations results, and another theoretical model, and good agreements between them were found. Thus, this analytical model can be used to design new SERS substrates and other possible optical sensors composed of metal nanocylinders.

Author Contributions: Conceptualization A.K.S. and A.I.; formal analysis, A.K.S., G.B. and A.I.; resources, A.K.S. and A.I.; software, A.K.S. and A.I.; supervision, A.K.S. and A.I.; visualization, A.K.S., G.B. and A.I.; writing—original draft, A.K.S., G.B. and A.I.; writing—review and editing, A.K.S., G.B. and A.I. All authors have read and agreed to the published version of the manuscript.

Funding: This work was supported by the Russian Science Foundation under Grant No. 23-19-00788, <https://rscf.ru/project/23-19-00788/> (accessed on 15 May 2023).

Institutional Review Board Statement: Not applicable.

Informed Consent Statement: Not applicable.

Data Availability Statement: The data are contained within the article.

Conflicts of Interest: The authors declare no conflict of interest.

References

1. Garcia-Vidal, F.J.; Pendry, J.B. Collective Theory for Surface Enhanced Raman Scattering. *Phys. Rev. Lett.* **1996**, *77*, 1163. [[CrossRef](#)]
2. Grésillon, S.; Aigouy, L.; Boccarda, A.C.; Rivoal, J.C.; Quelin, X.; Demarest, C.; Gadenne, P.; Shubin, V.A.; Sarychev, A.K.; Shalae, V.M. Experimental Observation of Localized Optical Excitations in Random Metal-Dielectric Films. *Phys. Rev. Lett.* **1999**, *82*, 4520. [[CrossRef](#)]
3. Ciraci, C.; Hill, R.T.; Mock, J.J.; Urzhumov, Y.; Fernandez-Dominguez, A.I.; Maier, S.A.; Pendry, J.B.; Chilkoti, A.; Smith, D.R. Probing the Ultimate Limits of Plasmonic Enhancement. *Science* **2012**, *337*, 1072–1074. [[CrossRef](#)]
4. Moreau, A.; Ciraci, C.; Mock, J.J.; Hill, R.T.; Wang, Q.; Wiley, B.J.; Chilkoti, A.; Smith, D.R. Controlled-Reflectance Surfaces with Film-Coupled Colloidal Nanoantennas. *Nature* **2012**, *492*, 86–89. [[CrossRef](#)]
5. Echtermeyer, T.J.; Britnell, L.; Jasnos, P.K.; Lombardo, A.; Gorbachev, R.V.; Grigorenko, A.N.; Geim, A.K.; Ferrari, A.C.; Novoselov, K.S. Strong Plasmonic Enhancement of Photovoltage in Graphene. *Nat. Commun.* **2011**, *2*, 458. [[CrossRef](#)]
6. Zhang, Y.; Grady, N.K.; Ayala-Orozco, C.; Halas, N.J. Three-Dimensional Nanostructures as Highly Efficient Generators of Second Harmonic Light. *Nano Lett.* **2011**, *11*, 5519–5523. [[CrossRef](#)]
7. Savage, K.J.; Hawkeye, M.M.; Esteban, R.; Borisov, A.G.; Aizpurua, J.; Baumberg, J.J. Revealing the quantum regime in tunnelling plasmonics. *Nature* **2012**, *491*, 574–577. [[CrossRef](#)]
8. Mertens, J.; Eiden, A.L.; Sigle, D.O.; Huang, F.; Lombardo, A.; Sun, Z.; Sundaram, R.S.; Colli, A.; Tserkezis, C.; Aizpurua, J.; et al. Controlling Subnanometer Gaps in Plasmonic Dimers Using Graphene. *Nano Lett.* **2013**, *13*, 5033–5038. [[CrossRef](#)]
9. Cai, H.; Wu, Y.; Dai, Y.; Pan, N.; Tian, Y.; Luo, Y.; Wang, X. Wafer scale fabrication of highly dense and uniform array of sub-5nm nanogaps for surface enhanced Raman scattering substrates. *Opt. Express* **2016**, *24*, 20808–20815. [[CrossRef](#)] [[PubMed](#)]
10. Mubeen, S.; Zhang, S.; Kim, N.; Lee, S.; Krämer, S.; Xu, H.; Moskovits, M. Plasmonic Properties of Gold Nanoparticles Separated from a Gold Mirror by an Ultrathin Oxide. *Nano Lett.* **2012**, *12*, 2088–2094. [[CrossRef](#)] [[PubMed](#)]
11. Chikkaraddy, R.; Zheng, X.; Benz, F.; Brooks, L.J.; de Nijs, B.; Carnegie, C.; Kleemann, M.E.; Mertens, J.; Bowman, R.W.; Vandenbosch, G.; et al. How Ultranarrow Gap Symmetries Control Plasmonic Nanocavity Modes: From Cubes to Spheres in the Nanoparticle-on-Mirror. *ACS Photonics* **2017**, *4*, 469–475. [[CrossRef](#)]
12. Chikkaraddy, R.; Turek, V.A.; Kongsuwan, N.; Benz, F.; Carnegie, C.; van de Goor, T.; de Nijs, B.; Demetriadou, A.; Hess, O.; Keyser, U.F.; et al. Mapping Nanoscale Hotspots with Single-Molecule Emitters Assembled into Plasmonic Nanocavities Using DNA Origami. *Nano Lett.* **2018**, *18*, 405–411. [[CrossRef](#)]

13. Demetriadou, A.; Hamm, J.M.; Luo, Y.; Pendry, J.B.; Baumberg, J.J.; Hess, O. Spatiotemporal Dynamics and Control of Strong Coupling in Plasmonic Nanocavities. *ACS Photonics* **2017**, *4*, 2410–2418. [[CrossRef](#)]
14. Yang, Y.; Kim, H.; Badloe, T.; Rho, J. Gap-plasmon-driven spin angular momentum selection of chiral metasurfaces for intensity-tunable metaholography working at visible frequencies. *Nanophotonics* **2022**, *11*, 4123–4133. [[CrossRef](#)]
15. Khorashad, L.K.; Argyropoulos, C. Unraveling the temperature dynamics and hot electron generation in tunable gap-plasmon metasurface absorbers. *Nanophotonics* **2022**, *11*, 4037–4052. [[CrossRef](#)]
16. Yezekyan, T.; Zenin, V.A.; Beermann, J.; Bozhevolnyi, S.I. Anapole States in Gap-Surface Plasmon Resonators. *Nano Lett.* **2022**, *22*, 6098–6104. [[CrossRef](#)]
17. Fu, Q.; Zhan, Z.; Dou, J.; Zheng, X.; Xu, R.; Wu, M.; Lei, Y. Highly Reproducible and Sensitive SERS Substrates with Ag Inter-Nanoparticle Gaps of 5 nm Fabricated by Ultrathin Aluminum Mask Technique. *ACS Appl. Mater. Interfaces* **2015**, *7*, 13322–13328. [[CrossRef](#)]
18. Jiang, T.; Chen, G.; Tian, X.; Tang, S.; Zhou, J.; Feng, Y.; Chen, H. Construction of Long Narrow Gaps in Ag Nanoplates. *J. Am. Chem. Soc.* **2018**, *140*, 15560–15563. [[CrossRef](#)]
19. Liu, G.; Liu, Y.; Liu, X.; Chen, J.; Fu, G.; Liu, Z. Large-area, low-cost, ultra-broadband, infrared perfect absorbers by coupled plasmonic-photonic micro-cavities. *Sol. Energy Mater. Sol. Cells* **2018**, *186*, 142–148. [[CrossRef](#)]
20. Lu, X.; Huang, Y.; Liu, B.; Zhang, L.; Song, L.; Zhang, J.; Zhang, A.; Chen, T. Light-Controlled Shrinkage of Large-Area Gold Nanoparticle Monolayer Film for Tunable SERS Activity. *Chem. Mater.* **2018**, *30*, 1989–1997. [[CrossRef](#)]
21. Ma, C.; Gao, Q.; Hong, W.; Fan, J.; Fang, J. Real-time probing nanopore-in-nanogap plasmonic coupling effect on silver supercrystals with surface-enhanced Raman spectroscopy. *Adv. Funct. Mater.* **2016**, *27*, 1–8. [[CrossRef](#)]
22. Nam, J.M.; Oh, J.W.; Lee, H.; Suh, Y.D. Plasmonic Nanogap-Enhanced Raman Scattering with Nanoparticles. *Acc. Chem. Res.* **2016**, *49*, 2746–2755. [[CrossRef](#)]
23. Pan, R.; Yang, Y.; Wang, Y.; Li, S.; Liu, Z.; Su, Y.; Quan, B.; Li, Y.; Gu, C.; Li, J. Nanocracking and metallization doubly-defined large-scale 3D plasmonic sub-10nm-gap arrays as extremely sensitive SERS substrate. *Nanoscale* **2018**, *10*, 3171–3180. [[CrossRef](#)]
24. Shin, Y.; Song, J.; Kim, D.; Kang, T. Facile preparation of ultrasmall void metallic nanogap from self-assembled gold-silica core-shell nanoparticles monolayer via kinetic control. *Adv. Mater.* **2015**, *27*, 4344–4350. [[CrossRef](#)]
25. Sigle, D.O.; Mertens, J.; Herrmann, L.O.; Bowman, R.W.; Ithurria, S.; Dubertret, B.; Shi, Y.; Yang, H.; Tserkezis, C.; Aizpurua, J.; et al. Monitoring Morphological Changes in 2D Monolayer Semiconductors Using Atom-Thick Plasmonic Nanocavities. *ACS Nano* **2015**, *9*, 825–830. [[CrossRef](#)]
26. Yoo, D.; Mohr, D.A.; Vidal-Codina, F.; John-Herpin, A.; Jo, M.; Kim, S.; Matson, J.; Caldwell, J.D.; Jeon, H.; Nguyen, N.-C.; et al. High-Contrast Infrared Absorption Spectroscopy via Mass-Produced Coaxial Zero-Mode Resonators with Sub-10 nm Gaps. *Nano Lett.* **2018**, *18*, 1930–1936. [[CrossRef](#)]
27. Zhou, J.; Xiong, Q.; Ma, J.; Ren, J.; Messersmith, P.B.; Chen, P.; Duan, H. A Polydopamine-Enabled Approach Toward Tailored Plasmonic Nanogapped Nanoparticles: From Nanogap Engineering to Multifunctionality. *ACS Nano* **2016**, *10*, 11066–11075. [[CrossRef](#)]
28. Bedingfield, K.; Elliott, E.; Gisdakis, A.; Kongsuwan, N.; Baumberg, J.J.; Demetriadou, A. Multi-faceted plasmonic nanocavities. *Nanophotonics* **2023**, *12*, 3931–3944. [[CrossRef](#)]
29. Gu, P.; Zheng, T.; Zhang, W.; Ai, B.; Zhao, Z.; Zhang, G. Sub-10 nm Au-Ag Heterogeneous Plasmonic Nanogaps. *Adv. Mater. Interfaces* **2020**, *7*, 1902021. [[CrossRef](#)]
30. Xomalis, A.; Zheng, X.; Demetriadou, A.; Martínez, A.; Chikkaraddy, R.; Baumberg, J.J. Interfering Plasmons in Coupled Nanoresonators to Boost Light Localization and SERS. *Nano Lett.* **2021**, *21*, 2512–2518. [[CrossRef](#)]
31. Li, Y.; Tang, S.; Xu, S.; Duan, Z.; Wang, Z.; Zhang, Y. Ag Nanoframes Deposited on Au Films Generate Optical Cavities for Surface-Enhanced Raman Scattering. *ACS Appl. Nano Mater.* **2020**, *3*, 5116–5122. [[CrossRef](#)]
32. Jagathpriya, L.; Pillanagrovi, J.; Dutta-Gupta, S. Tailoring cavity coupled plasmonic substrates for SERS applications. *Nanotechnology* **2023**, *34*, 335501.
33. Zhang, W.; Zheng, T.; Ai, B.; Gu, P.; Guan, Y.; Wang, Y.; Zhao, Z.; Zhang, G. Multiple plasmonic hot spots platform: Nanogap coupled gold nanoparticles. *Appl. Surf. Sci.* **2022**, *593*, 153388. [[CrossRef](#)]
34. Sarychev, A.K.; Sukhanova, A.; Ivanov, A.V.; Bykov, I.V.; Bakholdin, N.V.; Vasina, D.V.; Gushchin, V.A.; Tkachuk, A.P.; Nifontova, G.; Samokhvalov, P.S.; et al. Label-Free Detection of the Receptor-Binding Domain of the SARS-CoV-2 Spike Glycoprotein at Physiologically Relevant Concentrations Using Surface-Enhanced Raman Spectroscopy. *Biosensors* **2022**, *12*, 300. [[CrossRef](#)]
35. Ivanov, A.; Shalygin, A.; Lebedev, V.; Vorobev, V.; Vergiles, S.; Sarychev, A.K. Plasmonic extraordinary transmittance in array of metal nanorods. *Appl. Phys. A* **2012**, *107*, 17–21. [[CrossRef](#)]
36. Frumin, L.L.; Nemykin, A.V.; Perminov, S.V.; Shapiro, D.A. Plasmons excited by an evanescent wave in a periodic array of nanowires. *J. Opt.* **2013**, *15*, 085002. [[CrossRef](#)]
37. Liu, Z.Q.; Liu, G.Q.; Liu, X.S.; Huang, K.; Chen, Y.H.; Hu, Y.; Fu, G.L. Tunable plasmon-induced transparency of double continuous metal films sandwiched with a plasmonic array. *Plasmonics* **2013**, *8*, 1285–1292. [[CrossRef](#)]
38. Liu, G.Q.; Hu, Y.; Liu, Z.Q.; Chen, Y.H.; Cai, Z.J.; Zhang, X.N.; Huang, K. Robust multispectral transparency in continuous metal film structures via multiple near-field plasmon coupling by a finite-difference time-domain method. *Phys. Chem. Chem. Phys.* **2014**, *16*, 4320–4328. [[CrossRef](#)]

39. Liu, G.Q.; Hu, Y.; Liu, Z.Q.; Cai, Z.J.; Zhang, X.N.; Chen, Y.H.; Huang, K. Multispectral optical enhanced transmission of a continuous metal film coated with a plasmonic core-shell nanoparticle array. *Opt. Commun.* **2014**, *316*, 111–119. [[CrossRef](#)]
40. Rasskazov, I.L.; Markel, V.A.; Karpov, S.V. Transmission and spectral properties of short optical plasmon waveguides. *Opt. Spectrosc.* **2013**, *115*, 666–674. [[CrossRef](#)]
41. Klimov, V.V.; Guzatov, D.V. Strongly localized plasmon oscillations in a cluster of two metallic nanospheres and their influence on spontaneous emission of an atom. *Phys. Rev. B* **2007**, *75*, 24303. [[CrossRef](#)]
42. Klimov, V.; Guzatov, D. Plasmonic atoms and plasmonic molecules. *Appl. Phys. A* **2007**, *89*, 305–314. [[CrossRef](#)]
43. Guzatov, D.V.; Klimov, V.V. Optical properties of a plasmonic nano-antenna: An analytical approach. *New J. Phys.* **2011**, *13*, 053034. [[CrossRef](#)]
44. Lu, B.; Vegso, K.; Micky, S.; Ritz, C.; Bodik, M.; Fedoryshyn, Y.M.; Siffalovic, P.; Stemmer, A. Tunable Subnanometer Gaps in Self-Assembled Monolayer Gold Nanoparticle Superlattices Enabling Strong Plasmonic Field Confinement. *ACS Nano* **2023**, *17*, 12774–12787. [[CrossRef](#)]
45. Ding, F.; Yang, Y.; Deshpande, R.A.; Bozhevoyniy, S.I. A review of gap-surface plasmon metasurfaces: Fundamentals and applications. *Nanophotonics* **2018**, *7*, 1129–1156. [[CrossRef](#)]
46. Liu, W.; Lee, B.; Naylor, C.H.; Ee, H.S.; Park, J.; Johnson, A.C.; Agarwal, R. Strong Exciton–Plasmon Coupling in MoS₂ Coupled with Plasmonic Lattice. *Nano Lett.* **2016**, *16*, 1262–1269. [[CrossRef](#)]
47. Yang, L.; Xie, X.; Yang, J.; Xue, M.; Wu, S.; Xiao, S.; Song, F.; Dang, J.; Sun, S.; Zuo, Z.; et al. Strong Light–Matter Interactions between Gap Plasmons and Two-Dimensional Excitons under Ambient Conditions in a Deterministic Way. *Nano Lett.* **2022**, *22*, 2177–2186. [[CrossRef](#)]
48. Dong, L.; Yang, X.; Zhang, C.; Cerjan, B.; Zhou, L.; Tseng, M.L.; Zhang, Y.; Alabastri, A.; Nordlander, P.; Halas, N.J. Nanogapped Au Antennas for Ultrasensitive Surface-Enhanced Infrared Absorption Spectroscopy. *Nano Lett.* **2017**, *17*, 5768–5774. [[CrossRef](#)]
49. Paoletta, A.L.; Fung, E.-D.; Venkataraman, L. Gap Size-Dependent Plasmonic Enhancement in Electroluminescent Tunnel Junctions. *ACS Photonics* **2022**, *9*, 688–693. [[CrossRef](#)]
50. Dmitriev, P.A.; Lassalle, E.; Ding, L.; Pan, Z.; Neo, D.C.J.; Valuckas, V.; Paniagua-Dominguez, R.; Yang, J.K.W.; Demir, H.V.; Kuznetsov, A.I. Hybrid Dielectric-Plasmonic Nanoantenna with Multiresonances for Subwavelength Photon Sources. *ACS Photonics* **2023**, *10*, 582–594. [[CrossRef](#)]
51. Boroviks, S.; Lin, Z.-H.; Zenin, V.A.; Ziegler, M.; Dellith, A.; Gonçalves, P.A.D.; Wolff, C.; Bozhevolnyi, S.I.; Huang, J.-S.; Mortensen, N.A. Extremely confined gap plasmon modes: When nonlocality matters. *Nat. Commun.* **2022**, *13*, 3105. [[CrossRef](#)] [[PubMed](#)]
52. Kim, I.; Kim, H.; Han, S.; Kim, J.; Kim, Y.; Eom, S.; Barulin, A.; Choi, I.; Rho, J.; Lee, L.P. Metasurfaces-Driven Hyperspectral Imaging via Multiplexed Plasmonic Resonance Energy Transfer. *Adv. Mater.* **2023**, *35*, 2300229. [[CrossRef](#)] [[PubMed](#)]
53. Li, W.; Valentine, J.G. Harvesting the loss: Surface plasmon-based hot electron photodetection. *Nanophotonics* **2017**, *6*, 177–191. [[CrossRef](#)]
54. Barbillon, G.; Ivanov, A.; Sarychev, A.K. SERS Amplification in Au/Si Asymmetric Dimer Array Coupled to Efficient Adsorption of Thiophenol Molecules. *Nanomaterials* **2021**, *11*, 1521. [[CrossRef](#)]
55. Kneipp, J. Interrogating Cells, Tissues, and Live Animals with New Generations of Surface-Enhanced Raman Scattering Probes and Labels. *ACS Nano* **2017**, *11*, 1136–1141. [[CrossRef](#)]
56. Hu, Y.; Cheng, H.; Zhao, X.; Wu, J.; Muhammad, F.; Lin, S.; He, J.; Zhou, L.; Zhang, C.; Deng, Y.; et al. Surface-Enhanced Raman Scattering-Active Gold Nanoparticles with Enzyme Mimicking Activities for Measuring Glucose and Lactate in Living Tissues. *ACS Nano* **2017**, *11*, 5558–5566. [[CrossRef](#)]
57. Andreou, C.; Neuschmelting, V.; Tschaharganeh, D.F.; Huang, C.H.; Oseledchik, A.; Iacono, P.; Karabeber, H.; Colen, R.R.; Mannelli, L.; Lowe, S.W.; et al. Imaging of Liver Tumors Using Surface-Enhanced Raman Scattering Nanoparticles. *ACS Nano* **2016**, *10*, 5015–5026. [[CrossRef](#)]
58. Chon, H.; Lee, S.; Yoon, S.Y.; Lee, E.K.; Chang, S.L.; Choo, J. SERS-based competitive immunoassay of troponin I and CK-MB markers for early diagnosis of acute myocardial infarction. *Chem. Commun.* **2014**, *50*, 1058–1060. [[CrossRef](#)]
59. Boginskaya, I.A.; Slipchenko, E.A.; Sedova, M.V.; Zvyagina, J.Y.; Maximov, A.D.; Baburin, A.S.; Rodionov, I.A.; Merzlikin, A.M.; Ryzhikov, I.A.; Lagarkov, A.N. Additional Enhancement of Surface-Enhanced Raman Scattering Spectra of Myoglobin Precipitated under Action of Laser Irradiation on Self-Assembled Nanostructured Surface of Ag Films. *Chemosensors* **2023**, *11*, 321. [[CrossRef](#)]
60. Kraft, M.; Luo, Y.; Maier, S.A.; Pendry, J.B. Designing Plasmonic Gratings with Transformation Optics. *Phys. Rev. X* **2015**, *5*, 031029. [[CrossRef](#)]
61. Johnson, P.B.; Christy, R.W. Optical constants of the noble metals. *Phys. Rev. B* **1972**, *6*, 4370–4379. [[CrossRef](#)]
62. Luo, Y.; Fernandez-Dominguez, A.I.; Wiener, A.; Maier, S.A.; Pendry, J.B. Surface Plasmons and Nonlocality: A Simple Model. *Phys. Rev. Lett.* **2013**, *111*, 093901. [[CrossRef](#)]
63. Yue, W.; Wang, Z.; Whittaker, J.; Lopez-Royo, F.; Yang, Y.; Zayats, A.V. Amplification of surface-enhanced Raman scattering due to substrate-mediated localized surface plasmons in gold nanodimers. *J. Mater. Chem. C* **2017**, *5*, 4075–4084. [[CrossRef](#)]
64. Li, Z.; You, Q.; Li, J.; Zhu, C.; Zhang, L.; Yang, L.; Fang, Y.; Wang, P. Boosting Light–Matter Interaction in a Longitudinal Bonding Dipole Plasmon Hybrid Anapole System. *J. Phys. Chem. C* **2023**, *127*, 3594–3601. [[CrossRef](#)]

65. Chowdhury, S.N.; Simon, J.; Nowak, M.P.; Pagadala, K.; Nyga, P.; Fruhling, C.; Bravo, E.G.; Maćkowski, S.; Shalaev, V.M.; Kildishev, A.V.; et al. Wide-Range Angle-Sensitive Plasmonic Color Printing on Lossy-Resonator Substrates. *Adv. Opt. Mater.* **2023**, 2301678. . [[CrossRef](#)]
66. Kanipe, K.; Chidester, P.; Stucky, G.; Meinhart, C.; Moskovits, M. Properly Structured, Any Metal Can Produce Intense Surface Enhanced Raman Spectra. *J. Phys. Chem. C* **2017**, *121*, 14269–14273. [[CrossRef](#)]

Disclaimer/Publisher's Note: The statements, opinions and data contained in all publications are solely those of the individual author(s) and contributor(s) and not of MDPI and/or the editor(s). MDPI and/or the editor(s) disclaim responsibility for any injury to people or property resulting from any ideas, methods, instructions or products referred to in the content.